How to cite: *Angew. Chem. Int. Ed.* **2025**, e202510671
doi.org/10.1002/anie.202510671

Oxygen Reduction Reaction **Hot Paper**

Transforming Single-Atom Site to Dual-Atom Site in Fe–N–C Catalysts: A Universal Strategy for Enhancing Durability in Proton-Exchange Membrane Fuel Cells

Ruguang Wang, Jiaxin Guo, Jisi Li, Quanlu Wang, Zheng Lv, Cairong Gong, Caofeng Pan,* and Tao Ling**

Abstract: Fe–N–C catalyst is the most promising non-noble metal oxygen reduction catalyst for proton-exchange membrane fuel cells (PEMFCs); however, their practical applications are still limited by unsatisfactory long-term stability. This is because the N atoms of the active FeN_4 moiety are easy to protonate, leading to the leaching of Fe atoms, and the H_2O_2 generated during oxygen reduction reaction (ORR) process triggers the Fenton reaction, further accelerating the dissolution of Fe. To address these critical stability challenge, we developed a general strategy to transform FeN_4 single-atom sites to Fe_2N_6 dual-atom sites in Fe–N–C catalysts with various carbon substrates. This is achieved by treating the presynthesized Fe–N–C catalysts in a H_2/Ar atmosphere to break the C—N bonds near the FeN_4 sites while introducing Fe and N precursors to form the Fe_2N_6 sites. Our theoretical calculations and experimental results demonstrate that the newly formed Fe_2N_6 sites are structurally more stable in acidic ORR and produce negligible H_2O_2 (<1%). Therefore, the transformed Fe–N–C catalyst exhibits an extremely low Fe demetalation ratio (0.61 at%) in 0.1 M $HClO_4$ after 80k cycling. More surprisingly, the transformed Fe–N–C catalyst can effectively decompose H_2O_2 with a high decomposition rate of 15.7 mmol min^{-1}, approaching that of the state-of-the art Pt/C catalyst (17 mmol min^{-1}). As a result, the transformed Fe–N–C catalyst assembled PEMFC operates stably for 300 h with only 7% current density attenuation, whereas that of the pristine Fe–N–C catalyst-based device declines by 84% within 100 h.

Introduction

The development of nonprecious metal-based catalysts is of great significance for the large-scale application of proton-exchange membrane fuel cells (PEMFCs).[1,2] Among various candidate materials, iron–nitrogen–carbon (Fe—N—C) single-atom catalysts have attracted much attention due to their oxygen reduction reaction (ORR) activity approaching that of commercial Pt/C catalysts.[3] At present, high performance Fe—N—C catalysts have been realized on various carbon supports, including polymer pyrolytic carbon,[4] carbon nanotubes,[5] commercial carbon black,[6] and metal–organic framework-derived carbon,[7] and single-atom Fe loading has exceeded 7 wt%.[8,9] Despite the significant progress, the industrial application of Fe—N—C catalysts in PEMFCs is limited by their unsatisfactory stability.[10,11] Specifically, in an acidic environment, the N atoms of the active FeN_4 sites are prone to protonation, causing the break of Fe—N bond and the leach of Fe atom.[12–14] Besides, ORR produces by-product hydrogen peroxide (H_2O_2), which further reacts with the leached Fe ions through the Fenton reaction, generating strong oxidative radicals that accelerate the dissolution of Fe atoms.[15–17] The above processes have been proven to be the main reasons for the rapid performance decline of PEMFCs in the initial operation stage (<100 h).

To address the critical stability of Fe—N—C catalyst in PEMFCs, some works demonstrated that Pt-based alloy nanoparticles[18,19] can effectively decompose H_2O_2 generated over the Fe—N—C catalyst, thus effectively avoiding the accumulation of H_2O_2 around the FeN_4 sites.[17,20,21] Similarly, radical scavengers, such as Ta-TiO_x[22] and CeO_2,[23,24] were introduced into the Fe—N—C catalyst layer to consume the radicals generated by the Fenton reaction, slowing down the degradation of the Fe—N—C catalyst. These works greatly promote the long-term stability of Fe—N—C catalysts and advance the application of Fe—N—C catalysts in PEMFCs. However, these strategies complicate the preparation of catalyst layer, and affect the mass transport at the three-phase interface, which undoubtedly increases the difficulty and cost for the actual application of PEMFCs.

On the other hand, the favorable pathway on Fe—N—C catalysts is $4e^-$ ORR through $O_2 \rightarrow *OOH \rightarrow *O \rightarrow *OH$, whereas *OOH is also the intermediate for $2e^-$ pathway ($O_2 \rightarrow *OOH \rightarrow H_2O_2$).[25] The key to promoting $4e^-$

[*] R. Wang, Dr. J. Guo, J. Li, Q. Wang, Z. Lv, Prof. C. Gong, Prof. T. Ling
Key Laboratory for Advanced Ceramics and Machining Technology of Ministry of Education, Tianjin Key Laboratory of Composite and Functional Materials, School of Materials Science and Engineering, Tianjin University, Tianjin 300072, China
E-mail: gcr@tju.edu.cn
lingt04@tju.edu.cn

Dr. J. Guo, Prof. C. Pan
Institute of Atomic Manufacturing, Beihang University, Beijing 100191, China
E-mail: pancaofeng@buaa.edu.cn

Additional supporting information can be found online in the Supporting Information section

ORR requires to break O—O bond in *OOH. Recently, it is suggested that *OOH adsorption on Fe–Fe dual-atom site[26–28] is a favorable bridge-type, whereas that on the Fe single-atom site is a terminal-type. This greatly accelerates the cleavage of the O—O bond and enhances the selectivity of $4e^-$ ORR. Therefore, it can be expected that if the Fe single-atom sites of Fe—N—C catalysts can be converted into Fe–Fe dual-atom configurations, the stability of Fe—N—C catalysts can be remarkably improved, which however remains unexplored yet. Notably, although Fe–Fe dual-atom catalysts have been successfully synthesized using bimetallic complexes as precursors,[29–31] the direct conversion of preformed Fe single-atom sites in Fe—N—C catalyst offers several practical advantages: 1) it builds upon well-established Fe—N—C synthesis protocols, 2) maintains compatibility with diverse carbon supports, and 3) preserves the high Fe loading capacity–all of which are advantageous for fuel cell applications.

Herein, we propose a general strategy to transform FeN_4 single-atom sites of Fe—N—C catalysts to Fe_2N_6 dual-atom sites, which is applicable to Fe—N—C catalysts with various carbon substrates, including polymer pyrolytic carbon, carbon nanotubes, commercial carbon black, and metal–organic framework-derived carbon. We show that the formation of Fe_2N_6 dual-atom sites remarkably improves the structural stability of Fe—N—C catalysts in acidic ORR, and significantly reduces the yield of H_2O_2. Therefore, the transformed Fe—N—C catalysts exhibit negligible Fe demetallization after 80k cycles of accelerated aging tests. More importantly, the transformed catalysts show strong H_2O_2 tolerance and can effectively decompose H_2O_2, similar to Pt/C. As a result, the assembled PEMFC works smoothly over 300 h at a constant voltage of 0.6 V, which is one of the highest durability records for nonprecious metal catalyst-based PEMFCs to date.

Results and Discussion

In this work, we aim to develop a general strategy for converting the single-atom sites in Fe—N—C catalysts to dual-atom sites (Figure 1a). Specifically, the presynthesized Fe—N—C catalyst was subjected to high-temperature treatment in H_2/Ar atmosphere to selectively break the C—N bonds near the FeN_4 sites; meanwhile, Fe and N precursors were introduced to form newly Fe–Fe dual-atoms (Figure S1). To confirm this conversion mechanism, we tested Fe—N—C, transformed Fe—N—C (T—Fe—N—C) catalysts and Fe—N—C catalyst treated in H_2/Ar atmosphere (without Fe and N precursors) using ^{13}C solid-state nuclear magnetic resonance spectroscopy (^{13}C ssNMR). As illustrated in Figure 1b, the Fe—N—C catalyst treated in H_2/Ar atmosphere exhibits significantly reduced intensities of C—N peaks at 45.6 and 53.9 ppm[32] compared to the Fe—N—C catalyst, along with a pronounced increase in C-defect as evidenced by the electron paramagnetic resonance (EPR), Raman spectroscopy, and C 1*s* X-ray photoelectron spectroscopy (XPS) (Figures S2 and S3). These observations indicate the cleavage of C—N bonds and the formation of C-vacancies, which provide the foundation for subsequent N and Fe doping. In contrast, the T—Fe—N—C catalyst, where Fe and N precursors were introduced during the H_2/Ar treatment, shows a substantial enhancement in C—N peak intensity (45.6 and 53.9 ppm) and a corresponding decrease in C-defect signals (Figures S2 and S3), demonstrating successful N incorporation and partial C-defect healing. XPS analysis of the N 1*s* spectrum further reveals a significant increase in Fe—N coordinated N intensity (Figure S4), confirming Fe—N formation during conversion. Notably, the conversion process preserves the catalyst's morphology (Figures S5–S7), whereas the slightly higher surface area of T—Fe—N—C (Figure S8) likely originates from H_2-induced selective etching of the carbon matrix during high-temperature treatment, generating additional micropores.

Moreover, we characterized Fe—N—C and T—Fe—N—C catalysts by aberration-corrected high-angle annular dark-field scanning transmission electron microscopy (HAADF-STEM). As shown in Figure 1c, Fe single-atom sites are uniformly dispersed in the Fe—N—C catalyst, whereas many Fe–Fe dual-atom sites are observed in the T—Fe—N—C catalyst (Figures 1d and S9). Statistical analysis of dual-atom pairs reveals that the distance between neighboring atoms is ~2.5 Å (Figure S9). Further, our detailed elemental analysis reveals that the Fe–Fe dual atom sites account for ~80 at.% of the total Fe atoms on the T—Fe—N—C catalyst, with the remaining ~20 at.% of Fe present in the single-atom form (Figure S9). Inductively coupled plasma optical emission spectroscopy (ICP-OES) reveals that the Fe contents for Fe—N—C and T—Fe—N—C catalysts are 1.5 and 3.5 wt%, respectively.

Moreover, we characterized the Fe—N—C and T—Fe—N—C catalysts by Fe *K*-edge X-ray absorption near-edge structure (XANES) spectroscopy. As illustrated in Figures 1e and S10, the absorption edge shifts to lower energy for T—Fe—N—C compared to Fe—N—C, indicating a reduced Fe oxidation state, consistent with Fe 2p XPS results (Figure S11). This lowered oxidation state suggests the formation of Fe–Fe interactions in T—Fe—N—C catalyst. Further, the Fourier transformed (FT) extended X-ray absorption fine structure (EXAFS) were analyzed to reveal the coordination configuration of Fe—N—C and T—Fe—N—C catalysts. As shown in Figure 1f, the FT-EXAFS of the Fe—N—C catalyst shows a main peak at 1.50–1.60 Å, which can be attributed to Fe—N scattering in the first coordination shell (Figures S12 and S13; Table S1). For the T—Fe—N—C catalyst, another characteristic peak is observed at 2.57 Å (Figure 1g), which can be assigned to the scattering of Fe–Fe. Subsequently, the fitting of EXAFS (Figure S14) indicates that the coordination numbers of Fe—N and Fe—Fe were 4.3 and 0.8, respectively. Comparison of simulated and experimental Fe *K*-edge XANES spectra (Figure S15) further confirms the Fe_2N_6 configuration in T—Fe—N—C.

To further verify the above statement, we analyzed the mass fragments ejected by Fe—N—C and T—Fe—N—C catalysts under ion beam irradiation using time-of-flight secondary ion mass spectrometry (TOF-SIMS) (Figure 1h). The Fe—N—C catalyst shows evident peak assigned to the single-atom site fragment $[FeN_4]^-$. For the T—Fe—N—C catalyst, the intensity of the dual-atom site fragment $[Fe_2N_6]^-$ significantly increases compared with that of the Fe—N—C catalyst.

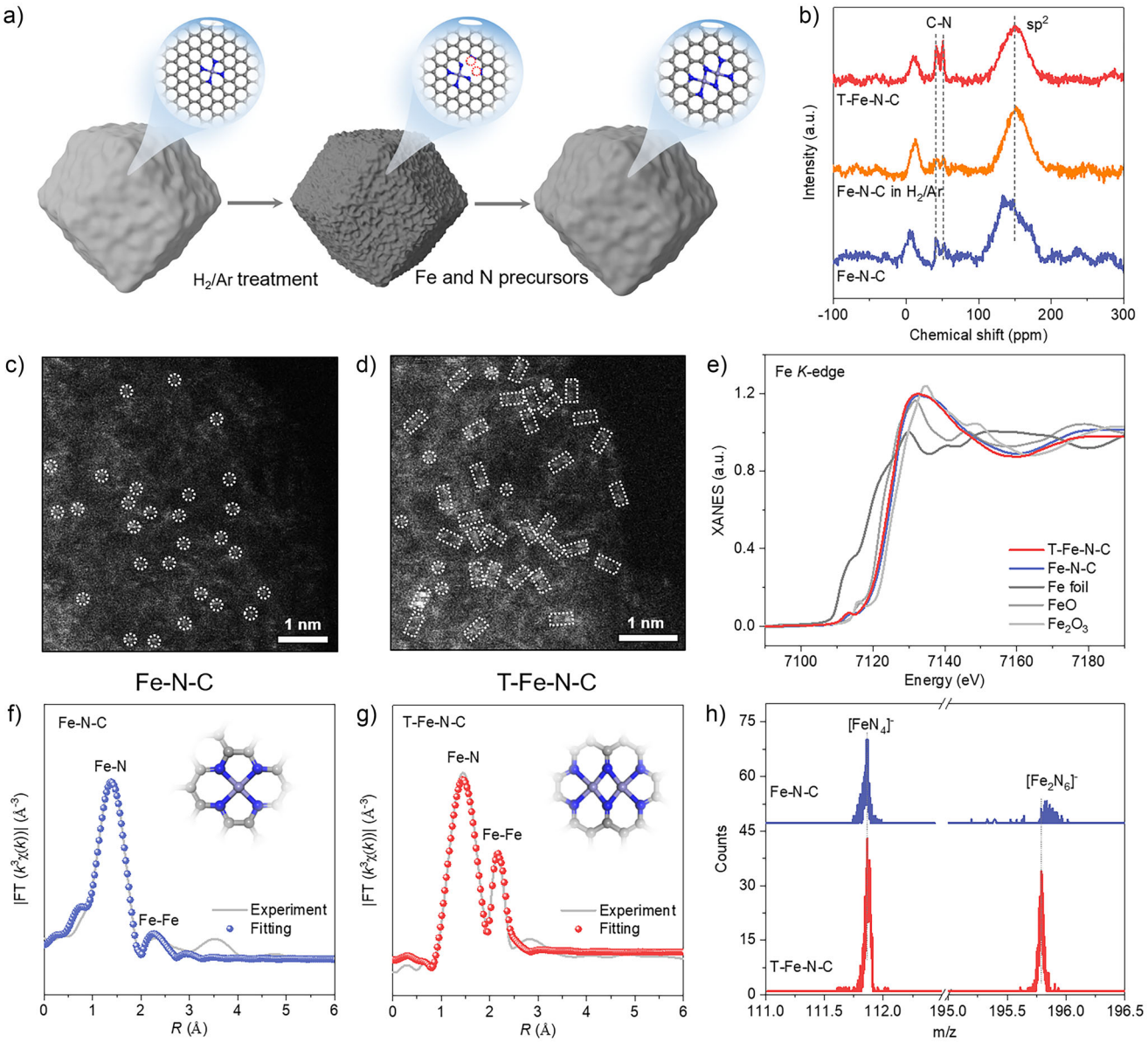

Figure 1. Synthesis and characterization of T—Fe—N—C catalyst. a) Schematic illustration showing the synthetic procedure to fabricate T—Fe—N—C catalyst. b) ^{13}C ssNMR spectra of catalysts. c) and d) HAADF-STEM image of Fe—N—C and T—Fe—N—C catalysts, respectively. Note that single-atom and dual-atom pairs in (c) and d) are denoted by dotted circles and rectangles, respectively. e) Fe *K*-edge XANES spectra of Fe—N—C, T—Fe—N—C, and reference samples. f) and g) FT k^3-weighted Fe *K*-edge EXAFS spectra and corresponding fitting curves for Fe—N—C and T—Fe—N—C, respectively. Insets: optimized structures (grey, blue, and lilac balls represent carbon, nitrogen, and iron atoms, respectively). h) TOF-SIMS spectra of Fe—N—C and T—Fe—N—C catalysts. The catalyst characterized in this figure is Fe—N—C_{ZIF}.

These collective characterization results confirm that the FeN_4 single-atoms sites in Fe—N—C catalyst can be transformed to dual-atom sites by our specifically designed strategy. We note that this strategy is applied to four carbon substrates-supported Fe—N—C catalysts, namely, polymer pyrolytic carbon (PC),[33] carbon nanotubes (CNTs),[5] commercial carbon black (CB),[6] and zeolitic imidazolate framework (ZIF)-derived carbon.[34] Despite their varying crystallinity and graphitization degrees (Figures S16 and S17), the transformation strategy consistently generated dual-atom sites in all systems, as confirmed by HAADF-STEM (Figure S18) and TOF-SIMS (Figure S19). Hereafter, these catalysts are referred to as Fe—N—C_{PC}, Fe—N—C_{CNT}, Fe—N—C_{CB}, and Fe—N—C_{ZIF}, and the transformed Fe—N—C catalysts are referred as T—Fe—N—C_{PC}, T—Fe—N—C_{CNT}, T—Fe—N—C_{CB}, and T—Fe—N—C_{ZIF}.

Afterward, we evaluated the ORR activities of the four Fe—N—C catalysts, and their corresponding transformed catalysts in O_2-saturated 0.1 M $HClO_4$ using a rotating ring disk electrode (RRDE). As illustrated in Figures 2a–d and S20, the half-wave potentials ($E_{1/2}$) of the four T—Fe—N—C catalysts were positively shifted compared with that of their corresponding Fe—N—C catalyst. Specifically, the $E_{1/2}$ of T—Fe—N—C_{CB}, T—Fe—N—C_{CNT}, T—Fe—N—C_{PC},

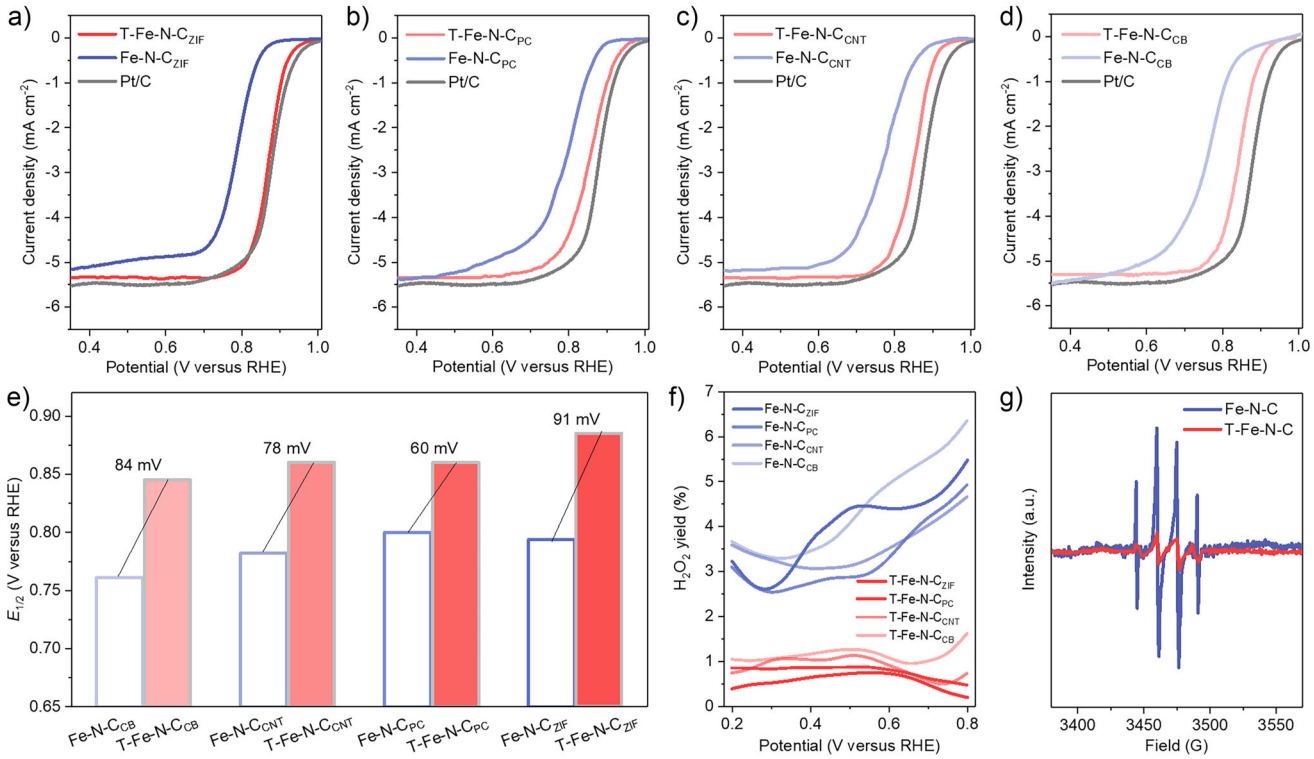

Figure 2. ORR performance of Fe—N—C and T—Fe—N—C catalysts. a)–d) Linear scan voltammogram (LSV) curves of Fe—N—C, T—Fe—N—C, and Pt/C catalysts in O_2-saturated 0.1 M $HClO_4$. e) $E_{1/2}$ of Fe—N—C and T—Fe—N—C catalysts. f) H_2O_2 yields of Fe—N—C and T—Fe—N—C catalysts. g) EPR spectra of the DMPO-•OH radical produced on Fe—N—C_{ZIF} and T—Fe—N—C_{ZIF} catalysts.

and T—Fe—N—C_{ZIF} were increased by 84, 78, 60, and 91 mV, respectively (Figure 2e). Evidently, T—Fe—N—C_{ZIF} exhibits the best performance, with an $E_{1/2}$ of 0.88 V versus reversible hydrogen electrode (V_{RHE}), approaching that of the state-of-the-art Pt/C catalyst ($E_{1/2} = 0.89$ V_{RHE}).

Moreover, after normalization by electrochemically active surface area (Figure S21), T—Fe—N—C catalysts display remarkably higher kinetic current densities compared to their Fe—N—C counterparts (Figure S22). This enhanced performance is further evidenced by their significantly higher turnover frequencies and mass activities (Figure S23), confirming the high intrinsic activity of the T—Fe—N—C catalysts. As expected, our in situ Raman spectroscopy (Figure S24) demonstrate that T—Fe—N—C enables bridge-mode oxygen adsorption and direct O—O bond cleavage, bypassing *OOH formation—an ideal mechanism for the 4e$^-$ ORR pathway.[26,30,35]

Next, we quantified the H_2O_2 yields of the Fe—N—C and T—Fe—N—C catalysts. As illustrated Figure 2f, the H_2O_2 yields of the four Fe—N—C catalysts are 3%–6% at 0.6 V_{RHE}, which are significantly decreased to less than 1% for the T—Fe—N—C catalysts under the identical conditions. Impressively, T—Fe—N—C_{ZIF} catalyst exhibits the lowest H_2O_2 yield of 0.2%–0.7% in the potential range of 0.2–0.8 V_{RHE}. Moreover, we compared the number of •OH radicals generated on the Fe—N—C_{ZIF} and T—Fe—N—C_{ZIF} catalysts through EPR, using 5,5-dimethyl-1-pyrroline-*N*-oxide (DMPO) as a spin trap. As shown in Figure 2g, the EPR spectra of both catalysts show characteristic 1:2:2:1 quartet patterns corresponding to DMPO-•OH adducts.[22] Strikingly, the T—Fe—N—C_{ZIF} catalyst exhibits >70% reduction in signal intensity relative to Fe—N—C_{ZIF} (Figure 2g), demonstrating its superior ability to suppress •OH radical generation during reaction.

Furthermore, the four T—Fe—N—C catalysts exhibit a significant improvement in stability compared with that of their corresponding Fe—N—C catalyst (Figures S25 and S26). Taking Fe—N—C_{ZIF} and T—Fe—N—C_{ZIF} catalysts as an example, as illustrated in Figure 3a,c, after 20k, 50k, and 80k cycling, the $E_{1/2}$ of the Fe—N—C_{ZIF} catalyst decreases by 24, 45, and 90 mV respectively, and the dissolution ratio of Fe is 8.21 at.%, 10.35 at.%, and 15.27 at.%, respectively. In contrast, for the T—Fe—N—C_{ZIF} catalyst, after 80k cycling, the $E_{1/2}$ remains unchangeable (Figure 3b), and the dissolution ratio of Fe is as low as 0.61 at.% (Figure 3c). Such excellent stability of the T—Fe—N—C catalyst outperforms ever reported Pt-free catalysts[7,12,22,26,36–44] (Table S2). Moreover, the T—Fe—N—C_{ZIF} catalyst exhibits only a 0.15% increase in H_2O_2 yield, comparable to Pt/C catalyst performance after 80k cycling (Figures S27 and S28). Meanwhile, under the constant voltage of 0.6 V_{RHE}, the current density of the Fe—N—C_{ZIF} catalyst drops by 40% after 30 h (Figure 3d), whereas that of the T—Fe—N—C_{ZIF} catalyst only decreases by 4.8% under the identical conditions.

To shed light on the above significantly enhanced stability of T—Fe—N—C catalysts, we performed density functional theory (DFT) calculations. According to previous works,[12,13] the performance degradation of Fe—N—C catalyst in acidic ORR is mainly due to the demetallization of the FeN_4 active

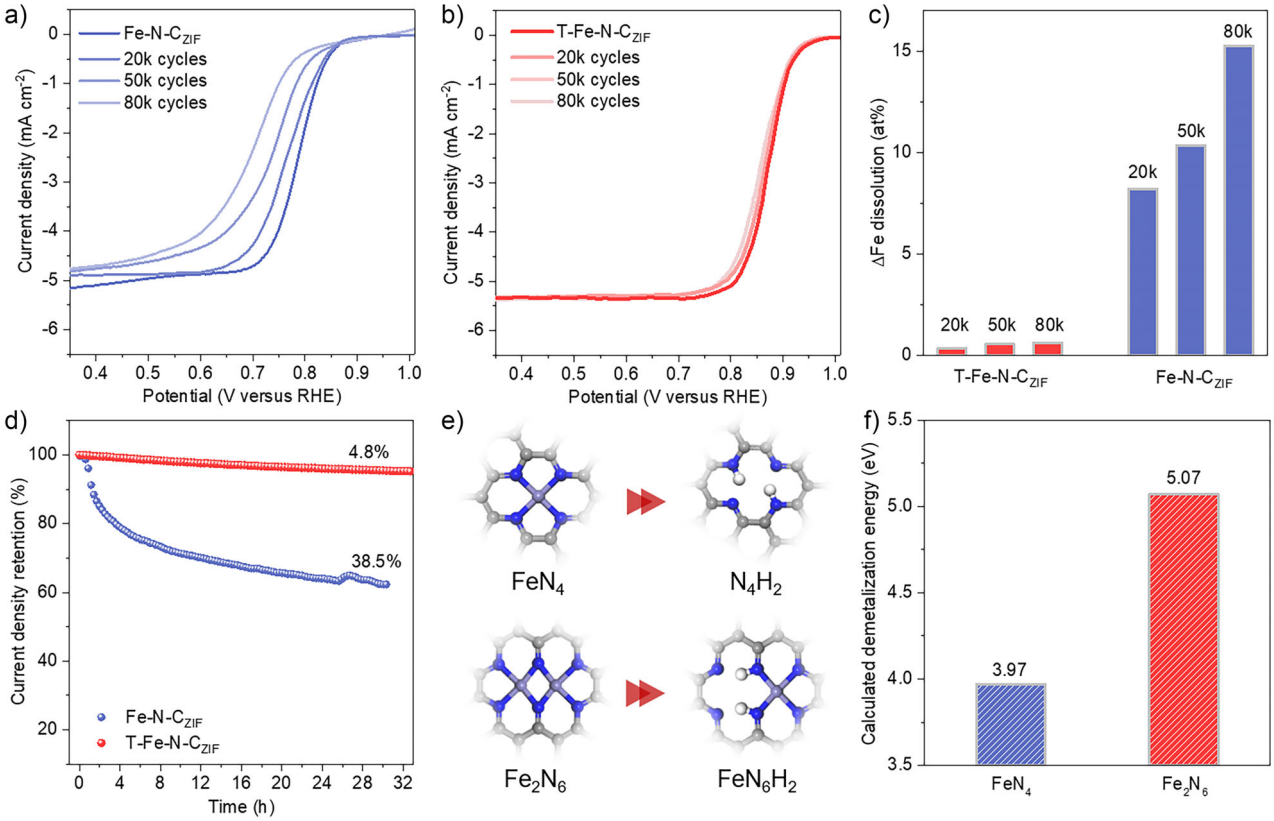

Figure 3. Stability of Fe—N—C and T—Fe—N—C catalysts in three-electrode setup. a) and b) LSV curves of Fe—N—C_{ZIF} and T—Fe—N—C_{ZIF} catalysts before and after different potential cycles between 0.6 and 1.0 V_{RHE} in O_2 saturated 0.1 M $HClO_4$ with a sweep rate at 10 mV s^{-1}, respectively. c) Measured dissolved ratios of Fe from Fe—N—C_{ZIF} and T—Fe—N—C_{ZIF} catalysts by ICP-OES after different potential cycles. d) Current density–time curves of Fe—N—C_{ZIF} and T—Fe—N—C_{ZIF} catalysts at 0.6 V_{RHE}. e) DFT-optimized structures and f) DFT-calculated demetallization of Fe from the FeN_4 and Fe_2N_6 sites shown in (e).

center, which occurs through protonation of the coordinated N atoms to form N—H groups, followed by the breakage of the Fe—N bond and the dissolution of Fe into the electrolyte. On this basis, we compared the energy costs of Fe demetallization from FeN_4 and Fe_2N_6 moieties (Figure 3e). As shown in Figure 3f, the energy cost of Fe demetallization from the Fe_2N_6 site is 5.07 eV, which is higher than that of the FeN_4 site (3.97 eV). This finding demonstrates that the Fe atoms is more stable in the Fe_2N_6 configuration, which can inhibit its demetallization in acidic environments. Besides, the ultralow H_2O_2 yield on T—Fe—N—C can effectively avoid the Fenton reaction and further slow down the Fe dissolution.

Besides structural unstability and high H_2O_2 yield, another factor limiting the practical application of Fe—N—C catalysts is that during PEMFC operation, even a small amount of H_2O_2 accumulates over time.[17,22] This triggers the Fenton reaction between dissolved Fe ions and H_2O_2, producing highly oxidative radicals that further exacerbates the dissolution of Fe, ultimately causing severe degradation of catalyst performance. Therefore, we compared the cycling stability of Fe—N—C_{ZIF} and T—Fe—N—C_{ZIF} catalysts when 50 mM H_2O_2 was added in 0.1 M $HClO_4$ electrolyte. As expected, after 10k cycling, the $E_{1/2}$ of the Fe—N—C_{ZIF} catalyst attenuates 82 mV (Figure 4a), with an Fe dissolution ratio of 17.3 at.% (Figure 4b). In sharp contrast, the $E_{1/2}$ of the T—Fe—N—C_{ZIF} decreases by only 10 mV (Figure 4a), whereas the Fe dissolution ratio is only 0.54 at.% (Figure 4b), indicating that T—Fe—N—C_{ZIF} has a strong tolerance to H_2O_2.

We found that the observed H_2O_2 tolerance of T—Fe—N—C_{ZIF} originates from its ability to decompose H_2O_2 (Figure S29). Specifically, we tested the H_2O_2 decomposition rate of Fe—N—C_{ZIF} and T—Fe—N—C_{ZIF} catalysts in 0.1 M $HClO_4$ containing 50 mM H_2O_2 under a constant potential of 0.6 V_{RHE}. Residual H_2O_2 concentration in the electrolyte was monitored using UV–visible (UV–Vis) spectroscopy every 2 min, and the decay curves were plotted (Figure 4c). For the T—Fe—N—C_{ZIF}, the H_2O_2 concentration drops rapidly to ~5 mM after 4 min, exhibiting a higher H_2O_2 decomposition rate (15.7 mmol min^{-1}), which approaches that of Pt/C catalyst (17 mmol min^{-1}) and is five times that of the Fe—N—C_{ZIF} catalyst. The decomposition process of H_2O_2 on Fe—N—C_{ZIF} and T—Fe—N—C_{ZIF} was also identified by time-dependent in situ Raman spectroscopy. As illustrated in Figure 4d, T—Fe—N—C_{ZIF} exhibits a distinct peak at 877 cm^{-1} (*O—O* stretching vibration of adsorbed H_2O_2),[45] whose intensity gradually decreases over time, whereas a new band emerges at ~1050 cm^{-1} (*OH stretching vibration).[46] Both features disappear after 6 min, demonstrating complete H_2O_2 decomposition. In contrast, no relative signals are observed on Fe—N—C_{ZIF} (Figure S30).

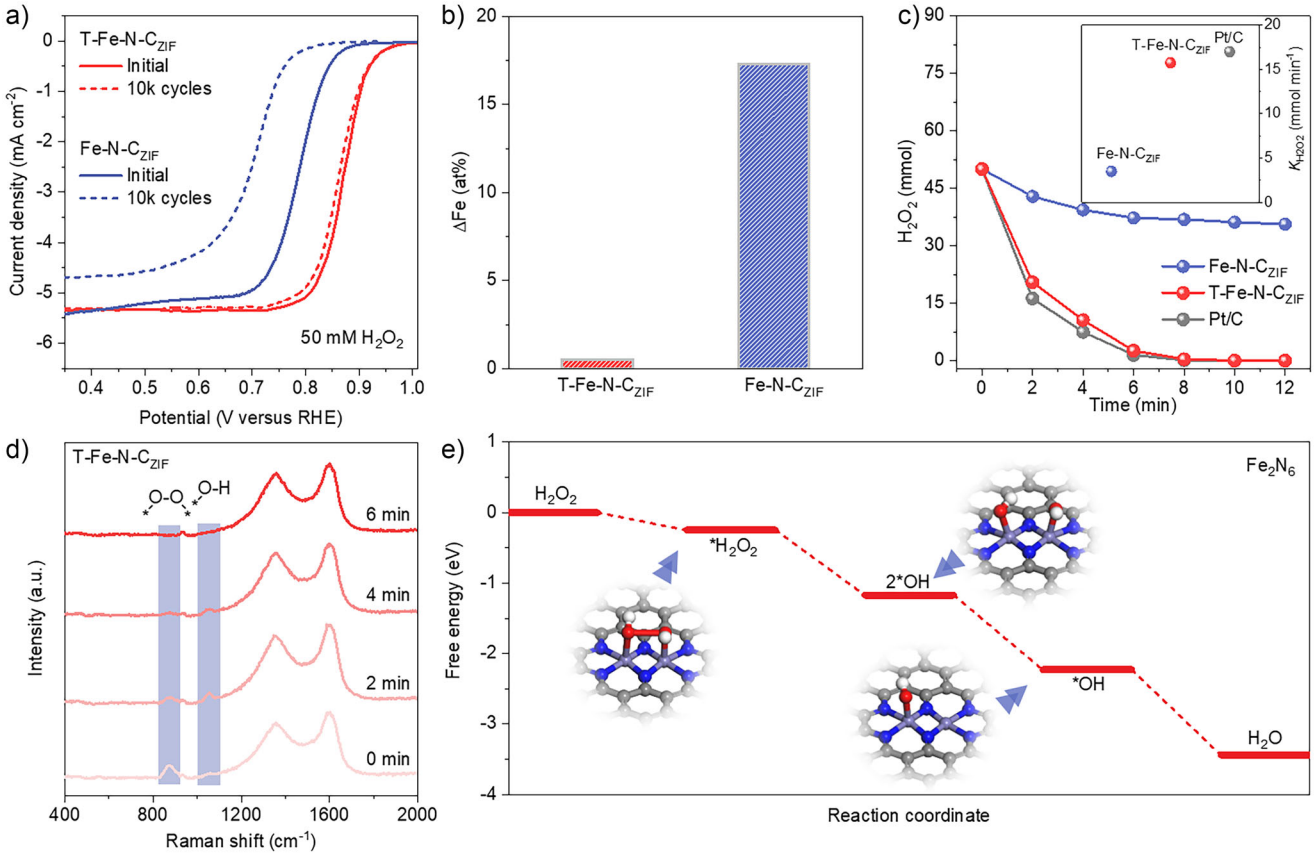

Figure 4. H_2O_2 tolerance of Fe—N—C and T—Fe—N—C catalysts. a) LSV curves of T—Fe—N—C_{ZIF} and Fe—N—C_{ZIF} catalysts at the initial cycle and after 10k cycles in O_2-saturated 0.1 M $HClO_4$ containing 50 mM H_2O_2. b) Measured dissolved ratios of Fe from Fe—N—C_{ZIF} and T—Fe—N—C_{ZIF} catalysts by ICP-OES after 10k cycles. c) Dynamic variation of H_2O_2 concentration over time for Fe—N—C_{ZIF}, T—Fe—N—C_{ZIF}, and Pt/C catalysts, with the inset showing corresponding H_2O_2 decomposition rate. d) Time-dependent in situ Raman spectra of T—Fe—N—C_{ZIF} catalyst at 0.6 V_{RHE}. e) DFT-calculated decomposition of H_2O_2 on T—Fe—N—C catalyst, with the inset showing the computed structures of intermediates adsorbed on T—Fe—N—C catalyst.

These results indicate that the T—Fe—N—C catalyst can effectively decompose H_2O_2, which was further elucidated by our DFT calculations. As revealed in Figure 4e, H_2O_2 adopts a favorable bridge-type adsorption configuration on the Fe–Fe dual-atom sites, subsequently dissociating into two *OH intermediates before final reduction to H_2O. The entire process is exothermic and can proceed spontaneously.

The above results demonstrate that the T—Fe—N—C_{ZIF} catalyst is structurally stable in acidic environments with ultralow H_2O_2 yield. Meanwhile, it can effectively decompose H_2O_2 accumulated during operation, which enables its promising application in PEMFCs. Subsequently, we assembled a PEMFC using T—Fe—N—C_{ZIF} and Pt/C catalysts as cathode and anode catalysts, respectively. For reference, Fe—N—C_{ZIF}-based PEMFC was also assembled. As illustrated in Figure 5a, under H_2-O_2 conditions, the T—Fe—N—C_{ZIF}-based PEMFC achieves a current density of 25 mA cm^{-2} at a cell voltage of 0.9 V, close to the target of the US Department of Energy (DOE)[47] in 2025 (44 mA cm^{-2}). Meanwhile, under 1.0 bar H_2–air conditions (Figure 5b), this PEMFC reaches a peak power density of 512 mW cm^{-2}, significantly higher than that of the Fe—N—C_{ZIF}-based device.

Moreover, we tested the long-term stability of the Fe—N—C_{ZIF} and T—Fe—N—C_{ZIF}-based PEMFCs under a constant cell voltage of 0.6 V in 1.0 bar H_2–air. As shown in Figure 5c, the T—Fe—N—C_{ZIF}-based PEMFC can work stably for more than 300 h, maintaining 93% of its initial current density. This makes it one of the most stable systems reported for Fe—N—C catalysts (Table S3). In contrast, the current density of the Fe—N—C_{ZIF}-based PEMFC decreases by 84% within 100 h. Moreover, we conducted accelerated durability tests (ADT) on the two PEMFCs, using a voltage wave to simulate automotive drive cycles (steps between 0.6 V (3 s) and 0.95 V (3 s) with a rise time of ~0.5 s). As shown in Figure 5d, after 10k and 30k cycling, the power density of the Fe—N—C_{ZIF}-based PEMFC decreases by 44% and 68%, respectively, whereas that of the T—Fe—N—C_{ZIF}-based PEMFC decreases by only 7% and 19%, respectively (Figure S31).

Furthermore, note that in PEMFCs, free radicals generated by the Fenton reaction will attack fluorine-containing membrane/ion polymers, thereby triggering the release of fluorine ions.[20] To verify this, we measured the concentration of degraded fluoride in the water tank after the stability test. We found that for the T—Fe—N—C_{ZIF} -based PEMFC, the fluorine ion concentration was significantly lower than that of the Fe—N—C_{ZIF}-based PEMFC (Figure S32). These results are consistent with the aforementioned

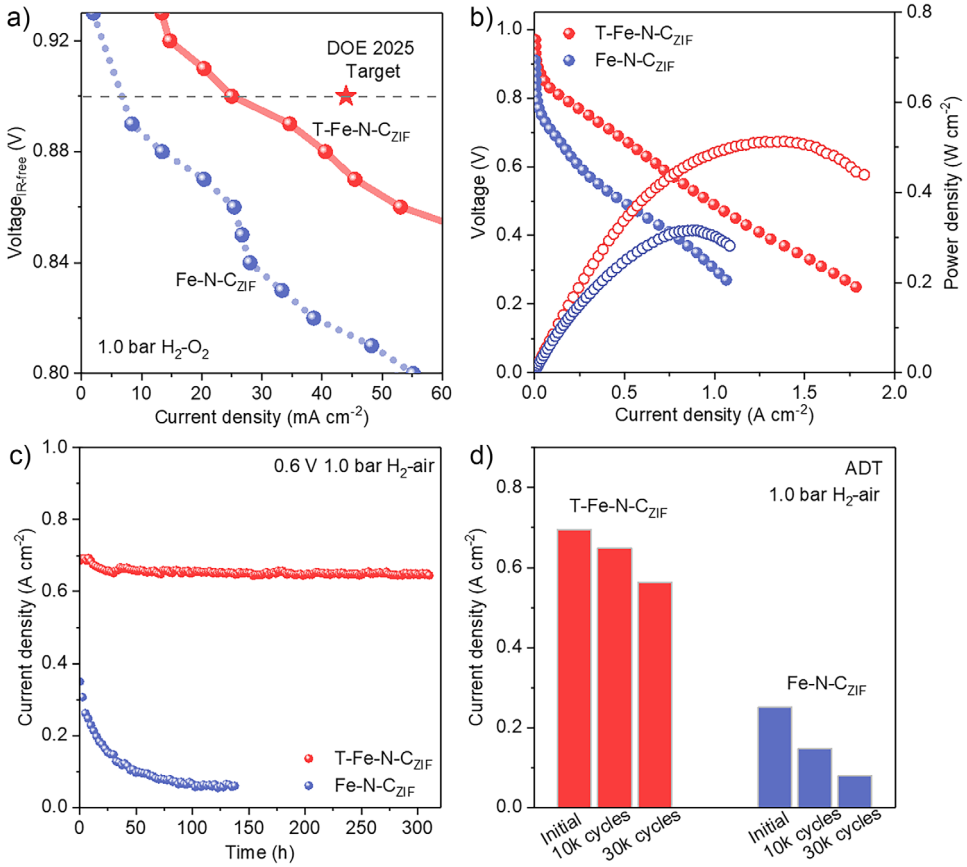

Figure 5. Performance and durability of Fe—N—C and T—Fe—N—C catalysts assembled PEMFCs. a) Performance at 0.9 $V_{iR\text{-}free}$ under 1 bar H_2–O_2. b) Polarization and power density curves. c) Long-term fuel cell tests under H_2–air conditions at a constant potential of 0.6 V. d) Current density decay at 0.6 V after the ADT test. Test conditions: cathode loading 4.0 mg cm^{-2} for T—Fe—N—C and Fe—N—C, anode loading 0.1 mg_{Pt} cm^{-2}, Nafion 212 membrane, 80 °C, 80 relative humidity, and 1.0 bar H_2–air or H_2–O_2 at flow rates of 300 mL min^{-1}.

theoretical and experimental findings, demonstrating that the Fe–Fe dual-atom sites in T—Fe—N—C_{ZIF} catalyst can reduce the generation of H_2O_2 and accelerate its decomposition. This dual functionality effectively inhibits the degradation of fluoride and improves the stability of assembled PEMFC.

Conclusion

In summary, we report a general strategy for transforming FeN_4 single-atom sites to Fe_2N_6 dual-atom sites in Fe—N—C catalysts with various carbon substrates. We demonstrate that the transformed catalysts are structurally stable, produce negligible H_2O_2, and more importantly, can effectively decompose H_2O_2. These characteristics endow the transformed Fe—N—C catalysts with surprising long-term stability in PEMFCs. We believe our work provides a direct guidance for addressing critical stability challenges of Fe—N—C catalysts for cost-effective and durable PEMFCs.

Acknowledgements

This work was supported by the National Natural Science Foundation of China (U23A2086 and 52071231).

Conflict of Interests

The authors declare no conflict of interest.

Data Availability Statement

The data that support the findings of this study are available in the Supporting Information of this article.

Keywords: Acidic oxygen reduction reaction · Coordination configuration · Metal demetallization · Platinum-free catalysts · Proton-exchange membrane fuel cells

[1] K. Jiao, J. Xuan, Q. Du, Z. Bao, B. Xie, B. Wang, Y. Zhao, L. Fan, H. Wang, Z. Hou, S. Huo, N. P. Brandon, Y. Yin, M. D. Guiver, *Nature* **2021**, *595*, 361–369.
[2] M. K. Debe, *Nature* **2012**, *486*, 43–51.
[3] G. Wu, P. Zelenay, *Nat. Rev. Mater.* **2024**, *9*, 643–656.
[4] G. Wu, K. L. More, C. M. Johnston, P. Zelenay, *Science* **2011**, *332*, 443–447.

[5] Y. J. Sa, D. J. Seo, J. Woo, J. T. Lim, J. Y. Cheon, S. Y. Yang, J. M. Lee, D. Kang, T. J. Shin, H. S. Shin, H. Y. Jeong, C. S. Kim, M. G. Kim, T. Y. Kim, S. H. Joo, *J. Am. Chem. Soc.* **2016**, *138*, 15046–15056.

[6] C. Ouyang, L. Zheng, Q. Zhang, X. Wang, *Adv. Mater.* **2022**, *34*, 2205372.

[7] H. Zhang, H. Sooyeon, W. Maoyu, F. Zhenxing, K. Stavros, L. Langli, Q. Zhi, X. Xiaohong, W. Chongmin, D. Su, S. Yuyan, W. Gang, *J. Am. Chem. Soc.* **2017**, *139*, 14143–14149.

[8] A. Mehmood, M. Gong, F. Jaouen, A. Roy, A. Zitolo, A. Khan, M.-T. Sougrati, M. Primbs, A. M. Bonastre, D. Fongalland, G. Drazic, P. Strasser, A. Kucernak, *Nat. Catal.* **2022**, *5*, 311–323.

[9] S. Yin, Y. Li, J. Yang, J. Liu, S. Yang, X. Cheng, H. Huang, R. Huang, C. T. Wang, Y. Jiang, S. Sun, *Angew. Chem. Int. Ed.* **2024**, *63*, e202404766.

[10] C. H. Choi, H.-K. Lim, M. W. Chung, G. Chon, N. Ranjbar Sahraie, A. Altin, M.-T. Sougrati, L. Stievano, H. S. Oh, E. S. Park, F. Luo, P. Strasser, G. Dražić, K. J. J. Mayrhofer, H. Kim, F. Jaouen, *Energy Environ. Sci.* **2018**, *11*, 3176–3182.

[11] L. Du, V. Prabhakaran, X. Xie, S. Park, Y. Wang, Y. Shao, *Adv. Mater.* **2020**, *33*, 1908232.

[12] S. Liu, C. Li, M. J. Zachman, Y. Zeng, H. Yu, B. Li, M. Wang, J. Braaten, J. Liu, H. M. Meyer, M. Lucero, A. J. Kropf, E. E. Alp, Q. Gong, Q. Shi, Z. Feng, H. Xu, G. Wang, D. J. Myers, J. Xie, D. A. Cullen, S. Litster, G. Wu, *Nat. Energy* **2022**, *7*, 652–663.

[13] J. Bai, T. Zhao, M. Xu, B. Mei, L. Yang, Z. Shi, S. Zhu, Y. Wang, Z. Jiang, J. Zhao, J. Ge, M. Xiao, C. Liu, W. Xing, *Nat. Commun.* **2024**, *15*, 4219.

[14] G. Bae, M. M. Kim, M. H. Han, J. Cho, D. H. Kim, M.-T. Sougrati, J. Kim, K.-S. Lee, S. H. Joo, W. A. Goddard, H.-S. Oh, H. Kim, F. Jaouen, C. H. Choi, *Nat. Catal.* **2023**, *6*, 1140–1150.

[15] Z. Miao, S. Li, C. Priest, T. Wang, G. Wu, Q. Li, *Adv. Mater.* **2022**, *34*, 2200595.

[16] Y. Zhao, P. Yin, Y. Yang, R. Wang, C. Gong, J. Li, J. Guo, Q. Wang, T. Ling, *Angew. Chem. Int. Ed.* **2025**, *64*, e202419501.

[17] H. Niu, L. Huang, Y. Qin, R. Qi, B. Mei, D. Wu, F.-M. Li, B. You, Q. Li, Y. Yao, Z. Wang, T. Yao, S. Ding, W. Guo, Y. Chen, Y. Su, F. Song, B. Y. Xia, *J. Am. Chem. Soc.* **2024**, *146*, 22650–22660.

[18] X. Ao, W. Zhang, B. Zhao, Y. Ding, G. Nam, L. Soule, A. Abdelhafiz, C. Wang, M. Liu, *Energy Environ. Sci.* **2020**, *13*, 3032–3040.

[19] S. Yin, Y.-N. Yan, L. Chen, N. Cheng, X. Cheng, R. Huang, H. Huang, B. Zhang, Y.-X. Jiang, S.-G. Sun, *ACS Nano* **2024**, *18*, 551–559.

[20] F. Xiao, Q. Wang, G.-L. Xu, X. Qin, I. Hwang, C.-J. Sun, M. Liu, W. Hua, H.-w. Wu, S. Zhu, J.-C. Li, J.-G. Wang, Y. Zhu, D. Wu, Z. Wei, M. Gu, K. Amine, M. Shao, *Nat. Catal.* **2022**, *5*, 503–512.

[21] D. Xue, Y. Yuan, Y. Yu, S. Xu, Y. Wei, J. Zhang, H. Guo, M. Shao, J.-N. Zhang, *Nat. Commun.* **2024**, *15*, 5990.

[22] H. Xie, X. Xie, G. Hu, V. Prabhakaran, S. Saha, L. Gonzalez-Lopez, A. H. Phakatkar, M. Hong, M. Wu, R. Shahbazian-Yassar, V. Ramani, M. I. Al-Sheikhly, D.-e. Jiang, Y. Shao, L. Hu, *Nat. Energy* **2022**, *7*, 281–289.

[23] X. Cheng, X. Jiang, S. Yin, L. Ji, Y. Yan, G. Li, R. Huang, C. Wang, H. Liao, Y. Jiang, S. Sun, *Angew. Chem. Int. Ed.* **2023**, *62*, e202306166.

[24] Y. Chu, E. Luo, Y. Wei, S. Zhu, X. Wang, L. Yang, N. Gao, Y. Wang, Z. Jiang, C. Liu, J. Ge, W. Xing, *Chem. Catal.* **2023**, *3*, 100532.

[25] T. Asset, P. Atanassov, *Joule* **2020**, *4*, 33–44.

[26] N. Zhang, T. Zhou, J. Ge, Y. Lin, Z. Du, C. a Zhong, W. Wang, Q. Jiao, R. Yuan, Y. Tian, W. Chu, C. Wu, Y. Xie, *Matter* **2020**, *3*, 509–521.

[27] Z. Xu, J. Zhu, J. Shao, Y. Xia, P. Liu, G. Li, R. Chen, S. Chen, J. Wang, S. Chen, F. Huang, H.-L. Wang, *Energy Environ. Sci.* **2024**, *17*, 8722–8733.

[28] Y. Yang, C. Hu, J. Shan, C. Cheng, L. Han, X. Li, R. Wang, W. Xie, Y. Zheng, T. Ling, *Angew. Chem. Int. Ed.* **2023**, *62*, e202300989.

[29] W. Ye, S. Chen, Y. Lin, L. Yang, S. Chen, X. Zheng, Z. Qi, C. Wang, R. Long, M. Chen, J. Zhu, P. Gao, L. Song, J. Jiang, Y. Xiong, *Chem* **2019**, *5*, 2865–2878.

[30] Y. X. Zhang, S. Zhang, H. Huang, X. Liu, B. Li, Y. Lee, X. Wang, Y. Bai, M. Sun, Y. Wu, S. Gong, X. Liu, Z. Zhuang, T. Tan, Z. Niu, *J. Am. Chem. Soc.* **2023**, *145*, 4819–4827.

[31] L. Yan, Y. Mao, Y. Li, Q. Sha, K. Sun, P. Li, G. I. N. Waterhouse, Z. Wang, S. Tian, X. Sun, *Angew. Chem. Int. Ed.* **2025**, *64*, e202413179.

[32] R. Jiang, L. Li, T. Sheng, G. Hu, Y. Chen, L. Wang, *J. Am. Chem. Soc.* **2018**, *140*, 11594–11598.

[33] Y. Chen, R. Gokhale, A. Serov, K. Artyushkova, P. Atanassov, *Nano Energy* **2017**, *38*, 201–209.

[34] R. Wang, L. Zhang, J. Shan, Y. Yang, J. F. Lee, T. Y. Chen, J. Mao, Y. Zhao, L. Yang, Z. Hu, T. Ling, *Adv. Sci.* **2022**, *9*, 2203917.

[35] L. Zhang, N. Zhang, H. Shang, Z. Sun, Z. Wei, J. Wang, Y. Lei, X. Wang, D. Wang, Y. Zhao, Z. Sun, F. Zhang, X. Xiang, B. Zhang, W. Chen, *Nat. Commun.* **2024**, *15*, 9440.

[36] S. Liu, M. Wang, X. Yang, Q. Shi, Z. Qiao, M. Lucero, Q. Ma, K. L. More, D. A. Cullen, Z. Feng, G. Wu, *Angew. Chem. Int. Ed.* **2020**, *59*, 21698–21705.

[37] G. Chen, Y. An, S. Liu, F. Sun, H. Qi, H. Wu, Y. He, P. Liu, R. Shi, J. Zhang, A. Kuc, U. Kaiser, T. Zhang, T. Heine, G. Wu, X. Feng, *Energy Environ. Sci.* **2022**, *15*, 2619–2628.

[38] J. Zhu, Z. Fang, X. Yang, M. Chen, Z. Chen, F. Qiu, M. Wang, P. Liu, Q. Xu, X. Zhuang, G. Wu, *ACS Catal.* **2022**, *12*, 6409–6417.

[39] Y. Qian, Q. Liu, E. Sarnello, C. Tang, M. Chng, J. Shui, T. Li, S. J. Pennycook, M. Han, D. Zhao, *ACS Mater. Lett.* **2019**, *1*, 37–43.

[40] S. Ding, J. A. Barr, Q. Shi, Y. Zeng, P. Tieu, Z. Lyu, L. Fang, T. Li, X. Pan, S. P. Beckman, D. Du, H. Lin, J.-C. Li, G. Wu, Y. Lin, *ACS Nano* **2022**, *16*, 15165–15174.

[41] J. Zou, C. Chen, Y. Chen, Y. Zhu, Q. Cheng, L. Zou, Z. Zou, H. Yang, *ACS Catal.* **2022**, *12*, 4517–4525.

[42] J. Li, W. Xia, J. Tang, Y. Gao, C. Jiang, Y. Jia, T. Chen, Z. Hou, R. Qi, D. Jiang, T. Asahi, X. Xu, T. Wang, J. He, Y. Yamauchi, *J. Am. Chem. Soc.* **2022**, *144*, 9280–9291.

[43] X. Fu, P. Zamani, J. Y. Choi, F. M. Hassan, G. Jiang, D. C. Higgins, Y. Zhang, M. A. Hoque, Z. Chen, *Adv. Mater.* **2017**, *29*, 1604456.

[44] J. Li, H. Zhang, W. Samarakoon, W. Shan, D. A. Cullen, S. Karakalos, M. Chen, D. Gu, K. L. More, G. Wang, Z. Feng, Z. Wang, G. Wu, *Angew. Chem. Int. Ed.* **2019**, *58*, 2–12.

[45] S. Ahmad, J. D. McCallum, A. K. Shiemke, E. H. Appelman, T. M. Loehr, J. Sanders-Loehr, *Inorg. Chem.* **1988**, *27*, 2230–2233.

[46] J.-C. Dong, X.-G. Zhang, V. Briega-Martos, X. Jin, J. Yang, S. Chen, Z.-L. Yang, D.-Y. Wu, J. M. Feliu, C. T. Williams, Z.-Q. Tian, J.-F. Li, *Nat. Energy* **2018**, *4*, 60–67.

[47] S. T. Thompson, A. R. Wilson, P. Zelenay, D. J. Myers, K. L. More, K. C. Neyerlin, D. Papageorgopoulos, *Solid State Ion* **2018**, *319*, 68–76.

Manuscript received: May 15, 2025
Revised manuscript received: June 15, 2025
Accepted manuscript online: June 20, 2025
Version of record online: ■■, ■■

Research Article

Oxygen Reduction Reaction

R. Wang, J. Guo, J. Li, Q. Wang, Z. Lv, C. Gong*, C. Pan*, T. Ling* — **e202510671**

Transforming Single-Atom Site to Dual-Atom Site in Fe–N–C Catalysts: A Universal Strategy for Enhancing Durability in Proton-Exchange Membrane Fuel Cells

This work develops a general strategy to transform FeN_4 single-atom sites to Fe_2N_6 dual-atom sites in Fe–N–C catalysts with various carbon substrates. Experimental evidence demonstrates that the transformed Fe–N–C catalyst exhibits highly active, selective, and strong H_2O_2 decomposition capability for proton-exchange membrane fuel cells.